

# THE NEAREST MILLISECOND PULSAR REVISITED WITH *XMM-NEWTON*: IMPROVED MASS-RADIUS CONSTRAINTS FOR PSR J0437–4715

SLAVKO BOGDANOV

Columbia Astrophysics Laboratory, Columbia University, 550 West 120th Street, New York, NY 10027, USA;  
 and Department of Physics, McGill University, 3600 University Street, Montreal, QC H3A 2T8, Canada;  
 slavko@astro.columbia.edu

*Draft version November 28, 2012*

## ABSTRACT

I present an analysis of the deepest X-ray exposure of a radio millisecond pulsar (MSP) to date, an *X-ray Multi Mirror-Newton* European Photon Imaging Camera spectroscopic and timing observation of the nearest known MSP, PSR J0437–4715. The timing data clearly reveal a secondary broad X-ray pulse offset from the main pulse by  $\sim 0.55$  in rotational phase. In the context of a model of surface thermal emission from the hot polar caps of the neutron star, this can be plausibly explained by a magnetic dipole field that is significantly displaced from the stellar center. Such an offset, if commonplace in MSPs, has important implications for studies of the pulsar population, high energy pulsed emission, and the pulsar contribution to cosmic ray positrons. The continuum emission shows evidence for at least three thermal components, with the hottest radiation most likely originating from the hot magnetic polar caps and the cooler emission from the bulk of the surface. I present pulse phase-resolved X-ray spectroscopy of PSR J0437–4715, which for the first time, properly accounts for the system geometry of a radio pulsar. Such an approach is essential for unbiased measurements of the temperatures and emission areas of polar cap radiation from pulsars. Detailed modelling of the thermal pulses, including relativistic and atmospheric effects, provides a constraint on the redshift-corrected neutron star radius of  $R > 11.1$  km (at  $3\sigma$  conf.) for the current radio timing mass measurement of  $1.76 M_{\odot}$ . This limit favors “stiff” equations of state.

*Subject headings:* pulsars: general — pulsars: individual (PSR J0437–4715) — stars: neutron — X-rays: stars — relativity

## 1. INTRODUCTION

PSR J0437–4715 was discovered by Johnston et al. (1993) in the Parkes southern radio pulsar survey. At a distance of  $156.3 \pm 1.3$  pc (Deller et al. 2008), it is the nearest known rotation-powered “recycled” millisecond pulsar (MSPs). It has properties typical of the Galactic population of MSPs, with a spin period  $P = 5.76$  ms and spin-down rate (after kinematic corrections) of  $\dot{P} \equiv dP/dt = 1.0 \times 10^{-20}$  s s<sup>−1</sup>, corresponding to a dipole magnetic field strength  $B = 3 \times 10^8$  G, a characteristic age  $\tau \approx 4.9$  Gyr, and spin-down luminosity  $\dot{E} = 3.8 \times 10^{33}$  ergs s<sup>−1</sup>. The pulsar is bound to a  $0.2 M_{\odot}$  white dwarf companion in a 5.74 day circular orbit (Bailyn 1993).

In soft X-rays, PSR J0437–4715 was the first MSP to be firmly detected, in a serendipitous discovery in the course of the *ROSAT* all sky survey (Becker & Trümper 1993). Subsequent observations with *ROSAT* (Becker & Trümper 1999), the *Extreme Ultraviolet Explorer* Deep Survey Instrument (Halpern et al. 1996), *Chandra* ACIS-S and HRC-S (Zavlin et al. 2002), and *XMM-Newton* EPIC MOS and pn (Zavlin 2006) revealed a single broad, asymmetric pulse and a relatively soft spectrum, with at least two distinct spectral components. The bulk of emission up to  $\sim 2$  keV is thermal in nature. The small inferred effective radii ( $\lesssim 2$  km) suggest that this radiation is associated with the neutron star polar caps. Given the large characteristic age of the pulsar, the heat is most likely not due to neutron star cooling but is instead

continuously supplied by an energetic return current from the magnetosphere above the polar caps (see, e.g., Harding & Muslimov 2002). Above  $\sim 2$  keV, Zavlin et al. (2002) have identified an additional faint component that is best described by a power-law. The nature of this spectral tail is less certain as it could be due to a variety of plausible mechanisms such as pulsed non-thermal radiation due to particle acceleration in the pulsar magnetosphere, unpulsed synchrotron radiation due to an unresolved, faint compact pulsar wind nebula or intrabinary shock, or a spectral tail caused by inverse Compton scattering of the soft thermal photons by particles (most likely electrons and positrons) of small optical depth (Bogdanov et al. 2006). PSR J0437–4715 has also been detected in the UV (Kargaltsev et al. 2004; Durant et al. 2012) and recently identified as a pulsed source in  $\gamma$ -rays ( $>100$  MeV) with the *Fermi* Large Area Telescope (Abdo et al. 2009).

Based on existing X-ray observations, modeling of the pulsed emission from PSR J0437–4715 has revealed unique insight into the properties of the stellar surface, magnetic field configuration, and neutron star structure. For instance, Pavlov & Zavlin (1997), Zavlin & Pavlov (1998), and Bogdanov et al. (2007) have demonstrated that a hydrogen atmosphere is likely present at the neutron star surface, as expected for a recycled pulsar (Alpar et al. 1982). The morphology of the thermal pulsations seen in the archival *XMM-Newton* data point to an offset of the magnetic axis from the neutron star center (Bogdanov et al. 2007). In addition, the compactness of PSR J0437–4715 is found to be  $R/R_S > 1.6$  (where

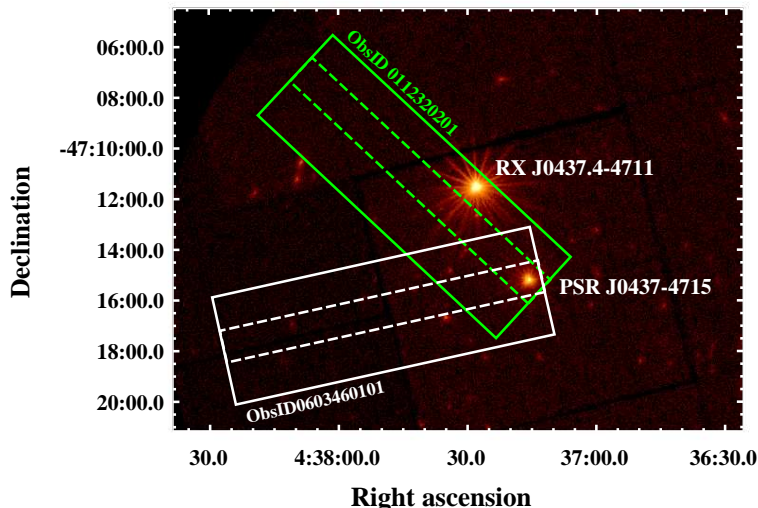


FIG. 1.— *XMM-Newton* MOS1 and MOS2 mosaic image of the field around PSR J0437–4715 in the 0.1–10 keV band. The rectangles show the relative positions and orientations of the active EPIC pn chip 4 used in observations 0603460101 (*white*) and 0112320201 (*green*), with the timing readout direction indicated by the arrow. The dashed lines delineate the EPIC pn detector columns used to extract the source counts from the pulsar. Note the significant contribution of photons from the background source RX J0437.4–4711 in the source extraction columns of observation 0112320201.

$R_S \equiv 2GM/c^2$  is the Schwarzschild radius) at 99.9% confidence, which for the best available mass measurement ( $1.76 \pm 0.20 M_\odot$  Verbiest et al. 2008) corresponds to  $R \gtrsim 8.3$  km (Bogdanov et al. 2007). As shown in Bogdanov et al. (2008), in principle, with deeper X-ray exposures it may be possible to obtain even tighter limits on the allowed neutron star equations of state. As the nearest and brightest known MSP, PSR J0437–4715 is the best-suited target for detailed investigation, especially given the availability of an independent mass measurement derived from radio timing observations. This combination can potentially provide stringent constraints on neutron star structure.

In this present paper, I report on a new *XMM-Newton* spectroscopic and timing observation of PSR J0437–4715, which sheds new light on the X-ray properties of MSPs and the physics of neutron stars, in general. The paper is organized as follows. In §2, I overview the observations and data reduction. In §3, I describe the characteristics of the pulse profile. In §4 and §5, I present phase-averaged and phase-resolved spectroscopic analyses of the pulsar. In §6, I present modelling the pulsed emission from PSR J0437–4715. I offer conclusions in §7.

## 2. OBSERVATION AND DATA REDUCTION

PSR J0437–4715 was revisited with *XMM-Newton* between 2009 December 15 and 17 (observation ID 0603460101) in a continuous 130-kilosecond exposure, corresponding to the entire available observing time of revolution 1835. The European Photon Imaging Camera (EPIC) MOS1/2 instruments were configured for full imaging mode. The EPIC pn was used in fast timing mode, in which only detector chip 4 is active, enabling 30  $\mu$ s relative timing precision while sacrificing one imaging dimension. For the MOS1/2 and pn, the thin optical filter was in place. The dispersed Reflection Grating Spectrometer (RGS) data yielded no interesting spectral or timing information, owing to the relatively faint nature of the pulsar, and were thus not used in this investigation.

The data reduction, imaging, and timing analyses were carried out using SAS<sup>1</sup> 10.0.0 and FTOOLS<sup>2</sup> 6.10, while the spectral analysis was conducted in XSPEC<sup>3</sup> 12.6.0q. The raw (ODF) MOS and pn datasets were reprocessed with the SAS *emchain* and *epchain* tools, respectively, and filtered for instances of strong background flares. Discarding time intervals with severely contaminated data results in 104.9, 104.9, and 120.4 ks of usable exposure time for MOS1, MOS2, and pn, respectively. Subsequently, the recommended processing filters (flag, pulse invariant, and pattern) were applied to generate the data used in the spectral and pulse profile analyses.

For the phase-integrated spectroscopy, the counts from the pulsar in the MOS 1/2 data were extracted from 60'' circles centered on the source position derived from radio timing (Verbiest et al. 2008), which contain  $\sim 90\%$  of the total energy at  $\sim 1.5$  keV. The background was estimated by considering three source-free regions in the immediate vicinity of the pulsar. For the phase-resolved spectroscopy and pulse profile modelling of the EPIC pn dataset, the counts from the MSP were obtained from RAWX columns 29–43 (inclusive), corresponding to a 30.75'' circle in full imaging mode, which encloses  $\sim 88\%$  of the total energy for 0.3–2 keV. This narrow extraction region was chosen so as to minimize the large background level (owing to the one-dimensional imaging mode used for the pn detector), which dominates beyond  $\sim 30''$  from the source position. To obtain a reliable estimate, the background was taken from source-free readout columns on both sides of the columns containing the pulsar. For the spectroscopic analysis of the EPIC MOS1/2 and pn data, the extracted counts were grouped using at least 30 and 150 counts per bin, respectively.

The archival *XMM-Newton* observation of PSR J0437–

<sup>1</sup> The *XMM-Newton* SAS is developed and maintained by the Science Operations Centre at the European Space Astronomy Centre and the Survey Science Centre at the University of Leicester.

<sup>2</sup> Available for download at <http://heasarc.gsfc.nasa.gov/ftools/>

<sup>3</sup> See <http://heasarc.nasa.gov/docs/xanadu/xspec/>

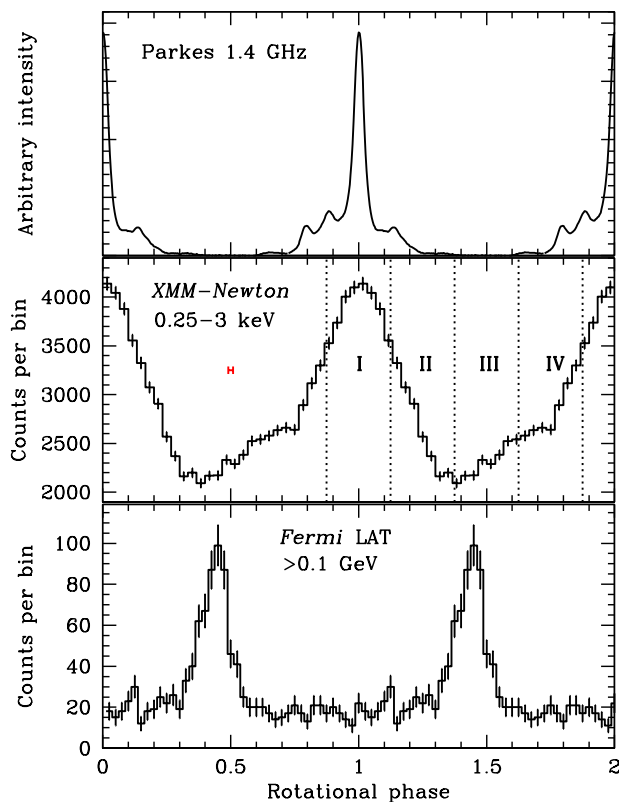


FIG. 2.— A comparison between the *XMM-Newton* EPIC pn X-ray pulse profile in the 0.3–2 keV range (*middle panel*), the template profile at 1.4 GHz (*top panel*), and the *Fermi* LAT profile (*bottom panel*) of PSR J0437–4715. Phase zero is defined based on the radio ephemeris. The error bar in the middle panel corresponds to the 70  $\mu$ s absolute timing uncertainty of *XMM-Newton*. The vertical dotted lines mark the phase intervals used in the phase-resolved spectroscopic analysis discussed in §5.

4715 (observation ID 0112320201, revolution 519), with the same instrument configuration as the new observation, was performed with an unfavorable mean telescope position angle ( $137^\circ$ ). As a consequence, the readout columns containing the pulsar emission are significantly contaminated by the background active galactic nucleus RX J0437.4–4711 (Halpern & Marshall 1996). In contrast, the new observation was carried out at a position angle that avoids the AGN entirely ( $192^\circ$ , see Figure 1) thus resulting in significant improvement in the quality of the timing data and a more reliable estimate of the background in the EPIC pn. In light of the problems with the archival data, the two EPIC pn observations were not combined and only the new, uncontaminated dataset was used.

### 3. PULSE PROFILE ANALYSIS

To obtain the X-ray pulse profile of PSR J0437–4715, the arrival times of the photons extracted from the pn source region (Fig. 1) were translated to the solar system barycenter with the *barycen* tool in SAS, assuming the pulsar position derived from radio timing (Verbiest et al. 2008) and the JPL DE405 solar system ephemeris. The corrected arrival times were folded at the radio ephemeris of PSR J0437–4715 from Verbiest et al. (2008) using the

TEMPO2<sup>4</sup> pulsar timing package. For an illustrative comparison, Figure 2 shows the radio, X-ray and  $\gamma$ -ray pulse profiles of PSR J0437–4715 all folded using the same ephemeris, hence showing the absolute phase alignment of the three pulse profiles.

Previous observations have uncovered that the X-ray pulsations from PSR J0437–4715 is characterized by a single broad and asymmetric peak that is significantly wider than the radio and  $\gamma$ -ray counterparts (Zavlin et al. 2002; Zavlin 2006). The substantial improvement in photon statistics of the new data clearly reveals a previously unseen “hump” at phases 0.5–0.75. For surface polar cap radiation, this feature likely corresponds to the secondary hot spot on the “far” side of the neutron star. The implied peak-to-peak separation of the two pulses in phase is  $\sim 0.55$  as measured from the more prominent to the fainter pulse, substantially different from 0.5 as expected from antipodal polar caps. This implies hot spots that are not diametrically opposite, presumably due to a significant offset of the magnetic dipole axis from the center of the star. Note that for PSR J0437–4715, the magnitude of the Doppler effect that would be induced by the rapid stellar rotation is not large enough to cause the apparent asymmetry, especially when a H atmosphere is assumed (see Figure 1 in Bogdanov et al. 2007).

The pulsed fraction (defined by convention as the portion of counts above the pulse minimum) of the background-subtracted lightcurves was determined from the pulse profile modelling presented in §6 in five energy bands: 0.275–0.35, 0.35–0.55, 0.55–0.75, 0.75–1.1, and 1.1–1.7 keV. This approach yields  $32\% \pm 1\%$ ,  $35\% \pm 1\%$ ,  $37\% \pm 1\%$ ,  $37\% \pm 1\%$ , and  $35\% \pm 2\%$ , respectively. It has been shown that for the range of plausible NS masses and radii, isotropic surface thermal emission from a neutron star surface, such as that due to a blackbody, cannot exceed  $\sim 33\%$  even from point-like hot spots for the plausible range of NS masses and radii (Psaltis et al. 2000; Beloborodov 2002). Nonetheless, the computed pulsed fractions are still in agreement with a predominantly thermal origin of the observed radiation if a H atmosphere is present on the neutron star surface. This is because the inherently anisotropic pattern of the emergent radiation from such an atmosphere can produce much larger rotation-induced modulations (see, e.g., Zavlin et al. 1996; Zavlin & Pavlov 1998). The slightly lower pulsed fraction at energies below  $\sim 0.35$  keV can be attributed to the contribution of emission from a larger portion of the stellar surface, as suggested by the UV emission from the pulsar (Durant et al. 2012) and the spectroscopic analysis in §4, which would be less modulated due to its greater physical extent. The pulse profiles for the other four energy bands are consistent with having identical pulsed fractions. Although the number of source photons is quite sparse above 2 keV, faint modulations similar to those at lower energies are seen in the 2–6 keV band. Closer inspection of the model spectrum shown in Figures 3, however, reveals a significant contribution from the hot thermal component, implying that the modulation may still be due to thermal emission. Unfortunately, due to the high background of the

<sup>4</sup> Available for download at <http://www.atnf.csiro.au/research/pulsar/tempo/>

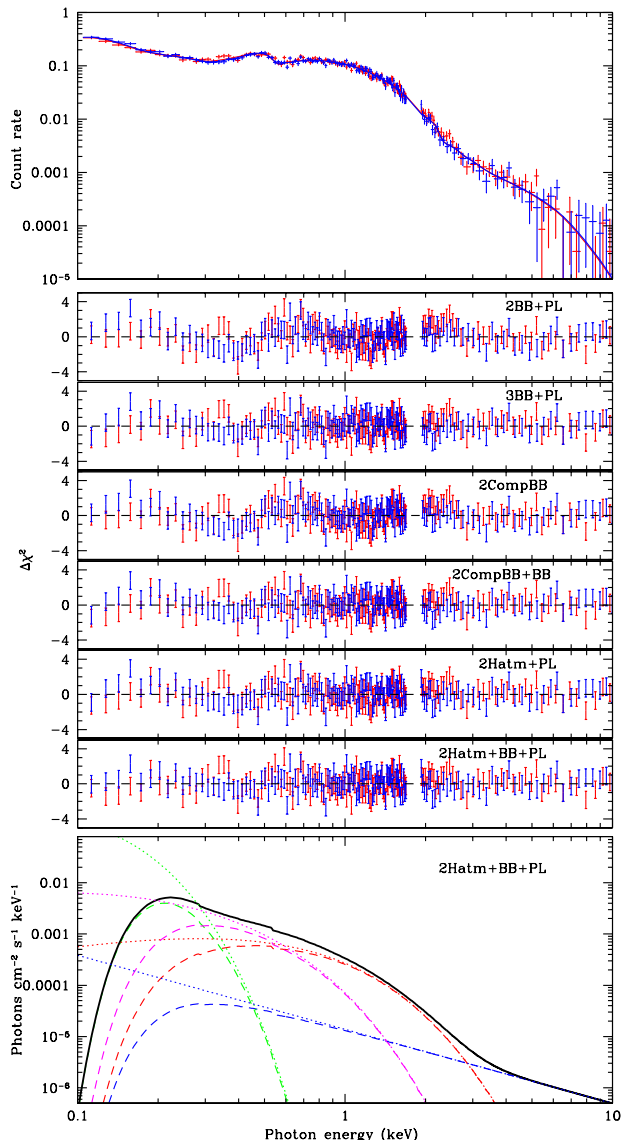


FIG. 3.— The *XMM-Newton* X-ray EPIC MOS1/2 spectra of PSR J0437–4715 fitted with a two-temperature H atmosphere model plus a power-law and a cool blackbody (solid line). The middle six panels show the fit residuals for the various models listed in Table 1. The bottom panel shows the best fit two-temperature H atmosphere model plus a power-law and a cool blackbody. The dashed and dotted lines show the individual absorbed and unabsorbed model components, respectively, while the solid line shows the total spectrum. See text and Table 1 for best fit parameters and acronym definitions.

EPIC pn data, combined with the significant decline in the telescope effective area at higher energies, no useful pulse profile information is available above  $\sim 3$  keV, where the contribution from the thermal components is negligible. Thus, only an uninteresting limit of  $\lesssim 90\%$  pulsed fraction for the background-subtracted emission can be placed, precluding any insight into the origin of the power-law tail.

#### 4. PHASE-AVERAGED SPECTROSCOPY

Zavlin et al. (2002) and Zavlin (2006) have found that the X-ray spectrum of PSR J0437–4715 cannot be adequately represented by a single or even most two compo-

nent emission models. Based on this, in the spectral fits I apply two plausible multi-component models: (i) a multi-temperature thermal plus single non-thermal model, and (ii) a multi-temperature Comptonized thermal model. For the thermal components, I consider both a simple blackbody and a non-magnetic H atmosphere spectrum (Romani 1987; Zavlin et al. 1996; McClintock et al. 2004), which is appropriate for PSR J0437–4715 given its low magnetic field ( $B \approx 3 \times 10^8$  G). Even though polar cap heating in MSPs is believed to be due to a return current of relativistic e from the magnetosphere above the polar caps, the H atmosphere model assumption of a heat source beneath the atmosphere is still fully valid. This is because the penetration depth of the impinging relativistic particles from the magnetosphere is much greater ( $\sim 2$ -3 orders of magnitude) than the characteristic depth of the atmosphere, meaning that their energy is deposited below the atmosphere (see Bogdanov et al. 2007, for details).

Blackbody fits to MSP spectra tend to produce inferred emission areas that are substantially smaller (a factor of  $\sim 10$ ) than the classical polar cap area,  $R_{pc} = (2\pi R/cP)^{1/2}R$ . In contrast, a H atmosphere yields values comparable to  $R_{pc}$  (Becker & Aschenbach 2002; Zavlin 2006; Bogdanov & Grindlay 2009). It has been suggested that the discrepancy for the blackbody model could be due to heating of only a small portion of the polar caps (Zhang & Cheng 2003). More plausibly, it suggests that an atmospheric layer is present on the stellar surface, as expected from evolutionary arguments. In particular, the peak intensity of a H atmosphere continuum occurs at higher energies than a blackbody for the same effective temperature. As a result, fitting a blackbody to H atmosphere emission would produce a higher inferred temperature and, as a result, a significantly smaller effective area. Furthermore, blackbody radiation has been shown to provide an inadequate description of the thermal pulsations from this MSP (Zavlin & Pavlov 1998; Bogdanov et al. 2007). Nevertheless, for completeness and to enable convenient comparison with previously published X-ray observations of MSPs, I have considered a blackbody in the spectroscopic analysis as well.

It is important to emphasize that even for phase-integrated spectroscopy it is essential to properly account for the rotation of the MSP and the geometric configuration of the hot spots, in order to obtain reliable measurements of the temperatures and emission radii (Psaltis et al. 2000; Zavlin et al. 2002; Bogdanov et al. 2007). For this reason, I consider the model of a rotating neutron star with two hot spots, based on the prescription described in Beloborodov (2002), Poutanen & Gierliński (2003), and Viironen & Poutanen (2004) but with the addition of a realistic H atmosphere (see Bogdanov et al. 2007, for further details). This model incorporates the angles between the spin and magnetic axes ( $\alpha$ ) and the spin axis and the line of sight ( $\zeta$ ) as well as the mass and radius of the pulsar as parameters in the spectral fits. Thus, the derived effective areas are deprojected and redshift-corrected. Moreover, the inferred temperatures are as measured at the NS surface by correcting them for gravitational redshift. For each polar cap I consider two concentric emission regions – a small high-temperature hot spot surrounded by a cooler an-

TABLE 1  
*XMM-Newton* EPIC MOS1/2 BEST-FIT SPECTRAL MODELS AND UNABSORBED FLUXES FOR PSR J0437–4715

Model <sup>a</sup>	$N_{\text{H}}$ ( $10^{19}$ cm $^{-2}$ )	$T_{\text{eff},1}$ ( $10^6$ K)	$R_{\text{eff},1}^b$ (km)	$T_{\text{eff},2}$ ( $10^6$ K)	$R_{\text{eff},2}^b$ (km)	$\Gamma$	$F_X^c$ (0.1–10 keV)	$\chi^2_{\nu}/\text{dof}$
BB( $\times 2$ )+PL	$5.7^{+1.7}_{-1.5}$ <0.09	$3.02^{+0.14}_{-0.12}$ $2.76^{+0.03}_{-0.05}$	$0.05^{+0.03}_{-0.02}$ $0.07^{+0.02}_{-0.01}$	$1.70^{+0.18}_{-0.16}$ $0.99^{+0.01}_{-0.04}$	$0.11^{+0.07}_{-0.06}$ $0.46^{+0.17}_{-0.11}$	-	$2.78^{+0.04}_{-0.07}$ 1.56	1.80(1.13) 1.34(0.20)
	7	$3.03^{+0.14}_{-0.12}$	$0.04^{+0.02}_{-0.02}$	$1.77^{+0.15}_{-0.13}$	$0.10^{+0.05}_{-0.04}$	-	$2.81^{+0.03}_{-0.03}$	1.88(1.25)
Hatm( $\times 2$ )+PL	$4.5^{+2.6}_{-2.2}$ $0.87^{+0.59}_{-0.55}$	$2.14^{+0.16}_{-0.11}$ $2.22^{+0.05}_{-0.04}$	$0.15^{+0.10}_{-0.06}$ $0.18^{+0.04}_{-0.05}$	$0.75^{+0.08}_{-0.08}$ $0.55^{+0.02}_{-0.01}$	$1.15^{+1.10}_{-0.78}$ $5.1^{+2.5}_{-3.5}$	-	$2.70^{+0.10}_{-0.24}$ 1.56	1.66(0.90) 1.41(0.15)
	7	$2.03^{+0.12}_{-0.11}$	$0.17^{+0.05}_{-0.05}$	$0.75^{+0.08}_{-0.08}$	$0.65^{+0.19}_{-0.25}$	-	$2.80^{+0.04}_{-0.03}$	1.85(1.20)
				$T_{\text{eff},3}$ ( $10^6$ K)	$R_{\text{eff},3}$ (km)			
BB( $\times 3$ )+PL	$18.2^{+4.8}_{-4.0}$ $16.7^{+5.5}_{-3.6}$	$3.16^{+0.11}_{-0.10}$ $3.21^{+0.09}_{-0.09}$	$0.05^{+0.02}_{-0.01}$ $0.04^{+0.02}_{-0.01}$	$1.51^{+0.08}_{-0.06}$ $1.54^{+0.06}_{-0.08}$	$0.21^{+0.11}_{-0.10}$ $0.21^{+0.12}_{-0.08}$	$0.44^{+0.06}_{-0.04}$ $0.46^{+0.02}_{-0.04}$	$4.6^{+4.8}_{-3.7}$ $4.0^{+3.5}_{-3.0}$	$1.78^{+0.35}_{-0.17}$ 1.56
	7	$3.20^{+0.08}_{-0.02}$	$0.04^{+0.02}_{-0.01}$	$1.57^{+0.09}_{-0.06}$	$0.19^{+0.07}_{-0.08}$	$0.53^{+0.04}_{-0.02}$	$1.9^{+0.9}_{-1.0}$	$1.73^{+0.35}_{-0.12}$
Hatm( $\times 2$ )	$16.7^{+8.2}_{-3.3}$	$2.56^{+0.06}_{-0.08}$	$0.17^{+0.03}_{-0.04}$	$1.00^{+0.03}_{-0.12}$	$1.3^{+0.6}_{-0.6}$	$0.42^{+0.06}_{-0.05}$	$4.9^{+7.9}_{-2.3}$	$1.12^{+0.43}_{-0.31}$
+BB+PL	$18.9^{+0.6}_{-0.6}$	$2.52^{+0.09}_{-0.09}$	$0.16^{+0.03}_{-0.03}$	$0.99^{+0.06}_{-0.22}$	$1.3^{+0.5}_{-0.7}$	$0.41^{+0.06}_{-0.04}$	$5.8^{+6.1}_{-4.8}$	1.56
	7	$2.56^{+0.06}_{-0.09}$	$0.17^{+0.05}_{-0.04}$	$1.04^{+0.12}_{-0.01}$	$1.1^{+1.1}_{-0.6}$	$0.48^{+0.02}_{-0.06}$	$2.1^{+2.2}_{-1.7}$	$1.15^{+0.43}_{-0.32}$
				$T_{\text{eff},3}$ ( $10^6$ K)	$R_{\text{eff},3}$ (km)	$\tau$		
CBB( $\times 2$ )	<0.1	$2.63^{+0.03}_{-0.05}$	$0.08^{+0.03}_{-0.02}$	$0.93^{+0.02}_{-0.03}$	$0.55^{+0.21}_{-0.14}$	-	-	$0.115^{+0.006}_{-0.005}$
CBB( $\times 2$ )+BB	$19.0^{+9.0}_{-7.0}$	$3.01^{+0.09}_{-0.08}$	$0.05^{+0.02}_{-0.02}$	$1.45^{+0.08}_{-0.06}$	$0.25^{+0.13}_{-0.12}$	$0.43^{+0.06}_{-0.5}$	$5.0^{+8.2}_{-3.2}$	$0.102^{+0.007}_{-0.008}$
	7	$3.03^{+0.11}_{-0.08}$	$0.05^{+0.02}_{-0.02}$	$1.49^{+0.10}_{-0.06}$	$0.22^{+0.09}_{-0.10}$	$0.52^{+0.04}_{-0.03}$	$1.95^{+1.05}_{-1.07}$	$0.109^{+0.007}_{-0.007}$

<sup>a</sup> PL is a powerlaw, BB a blackbody, CBB a Comptonized blackbody, and Hatm a non-magnetic H atmosphere model. All uncertainties and limits quoted are at a  $1\sigma$  confidence level.

<sup>b</sup>  $R_{\text{eff}}$  calculated assuming a distance of 156.3 pc. For the H atmosphere model, the numbers quoted represent deprojected and redshift-corrected effective radii of one hot spot on a neutron star with  $M = 1.76 M_{\odot}$ ,  $R = 13.5$  km,  $\alpha = 36^\circ$ ,  $\zeta = 42.4^\circ$ ,  $\Delta\alpha = -25^\circ$ , and  $\Delta\phi = -20^\circ$  (see text for definition of these parameters). The third, lowest temperature thermal component in all instances is a blackbody.

<sup>c</sup> Unabsorbed X-ray flux (0.1–10 keV) in units of  $10^{-13}$  ergs cm $^{-2}$  s $^{-1}$ . The values in parentheses represent the flux contribution of the powerlaw component, where applicable.

nular region, as implied by previous studies (Zavlin et al. 2002; Zavlin 2006). In all instances, to calculate effective radii, I consider the parallax distance of 156.3 pc (Deller et al. 2008). For the H atmosphere model, I assume a NS with  $M = 1.76 M_{\odot}$ ,  $R = 13.5$  km. I also fix  $\alpha = 36^\circ$  and  $\zeta = 42^\circ$  and account for the apparent offset of the secondary hot spot with the parameters  $\Delta\alpha = -25^\circ$  and  $\Delta\phi = -20^\circ$ , as deduced from the pulse profile fits (see §6). The various spectral models, their best fit parameters and derived unabsorbed fluxes are summarized in Table 1. All uncertainties quoted are given at a  $1\sigma$  confidence level. Following the analysis by Durant et al. (2012), the fits are performed with all parameters free, as well as with a fixed  $N_{\text{H}} = 7 \times 10^{19}$  cm $^{-2}$  or a fixed  $\Gamma = 1.56$ . The latter was found by Durant et al. (2012) to provide the best fit to the broadband non-thermal spectrum of this pulsar.

Regardless of the spectral model employed, fitting the phase-averaged MOS and pn datasets jointly results in statistically poor fits, with typical  $\chi_{\nu} \gtrsim 1.3$ . In contrast, the fits to either the MOS1/2 or pn data give  $\chi_{\nu} \lesssim 1.1$  for the same assumed models. This points to a possible discrepancy in the cross-calibration of the detectors especially for the fast timing mode of the EPIC pn instrument. Similar issues have been found in other studies using the pn fast timing mode (Zavlin 2006; Archibald et al. 2010). As a result, only the MOS 1/2 data were considered for the phase-averaged fits as they span a much wider energy range than the pn timing data. The MOS1/2 data exhibit significant narrow residuals at  $\sim 1.7$  keV. This feature can be attributed to the Si-K

edge<sup>5</sup>. Ignoring this interval results in significant improvement in the quality of the fits.

#### 4.1. Multi-Temperature Thermal Plus Powerlaw Spectrum

Based on previous *Chandra* and *XMM-Newton* observations, Zavlin et al. (2002), Zavlin (2006), and Durant et al. (2012) have reported that the phase-integrated X-ray radiation from PSR J0437–4715 is best represented by a two-temperature thermal plus a single faint powerlaw components. When applied to the new EPIC MOS1/2 data, the same model is only marginally acceptable and shows significant broad residuals at energies below  $\sim 0.8$  keV (middle panels in Figure 3), similar to those observed in *ROSAT* PSPC data (see Zavlin et al. 2002). This suggest the presence of an additional cool thermal component. The atmosphere model used in this study is only calculated down to  $T_{\text{eff}} = 3 \times 10^5$  K since below this temperature partial ionization becomes non-negligible (Zavlin et al. 1996; McClintock et al. 2004). As a consequence, the third, cool thermal component was represented by a blackbody. This addition results in a significant improvement in the fit quality.

Durant et al. (2012) have found that the spectral shape in the UV is consistent with thermal emission from the bulk of the NS surface with an effective temperature  $(1.5 - 3.5) \times 10^5$ . The MOS 1/2 fits suggest values in agreement with the upper bound of this range, although

<sup>5</sup> See <http://xmm2.esac.esa.int/docs/documents/CAL-TN-0018.pdf> for details.



TABLE 2  
EPIC PN RESULTS OF PHASE-RESOLVED SPECTROSCOPY FOR PSR J0437–4715.

Model <sup>a</sup>	$N_{\text{H}}$ ( $\text{cm}^{-2}$ )	$T_{\text{eff},1}$ ( $10^6$ K)	$R_{\text{eff},1}^b$ (km)	$T_{\text{eff},2}$ ( $10^6$ K)	$R_{\text{eff},2}^b$ (km)	$\Gamma$	$F_{\text{X}}^c$ (0.5–3 keV)	$\chi^2_{\nu}/\text{dof}$
BB( $\times 2$ )+PL	<12.5	$2.90^{+0.10}_{-0.11}$	$0.07^{+0.03}_{-0.03}$	$1.24^{+0.05}_{-0.06}$	$0.37^{+0.20}_{-0.18}$	$-0.14^{+1.38}_{-1.77}$	9.4/6.0/4.9/6.4	1.02/480
	<7.9	$2.82^{+0.08}_{-0.04}$	$0.07^{+0.03}_{-0.03}$	$1.22^{+0.06}_{-0.06}$	$0.37^{+0.19}_{-0.19}$	1.56	9.3/6.0/4.9/6.4	1.02/481
	7	$2.90^{+0.05}_{-0.06}$	$0.07^{+0.02}_{-0.02}$	$1.23^{+0.05}_{-0.06}$	$0.39^{+0.17}_{-0.14}$	$-0.11^{+1.67}_{-1.74}$	9.6/6.1/5.0/6.6	1.02/481
Hatm( $\times 2$ )+PL	<4.3	$2.22^{+0.04}_{-0.09}$	$0.16^{+0.07}_{-0.04}$	$0.55^{+0.05}_{-0.08}$	$6.0^{+6.0}_{-2.4}$	$2.35^{+0.17}_{-0.20}$	9.3/6.1/4.9/6.2	1.06/486
	<1.5	$2.16^{+0.05}_{-0.07}$	$0.18^{+0.08}_{-0.06}$	$0.58^{+0.05}_{-0.05}$	$5.1^{+6.7}_{-3.6}$	1.56	9.5/6.1/4.8/6.2	1.07/487
	7	$2.21^{+0.08}_{-0.10}$	$0.16^{+0.06}_{-0.05}$	$0.57^{+0.05}_{-0.08}$	$5.5^{+5.9}_{-3.5}$	$2.39^{+0.32}_{-0.18}$	9.6/6.3/5.0/6.3	1.06/487

<sup>a</sup> Model and parameter definitions are the same as in Table 1.

<sup>b</sup> For the blackbody fits, the quoted effective radius is that measured at pulse maximum (corresponding to phase interval I in Figure 2). For the H atmosphere, the value is the true, deprojected and redshift-corrected effective radius.

<sup>c</sup> Unabsorbed X-ray fluxes (0.5–3 keV) in units of  $10^{-13}$  ergs  $\text{cm}^{-2}$   $\text{s}^{-1}$  for the four phase bins.

the generally higher values may also indicate a temperature gradient across the stellar surface, possibly as a function of distance from the heated polar caps.

#### 4.2. Comptonized Thermal Spectrum

As suggested in Bogdanov et al. (2006), the power-law tail observed in the spectrum of PSR J0437–4715 may arise due to inverse Compton scattering (ICS) of the thermal X-ray radiation by relativistic  $e^{\pm}$  of small optical depth. It is plausible to assume that such particles may be located in the magnetosphere above the polar caps. For the spectroscopic analysis of PSR J0437–4715, I use the `compbb` Comptonized blackbody model in `XSPEC` (Nishimura et al. 1986). As additional parameters, this model includes a scattering particle temperature  $kT_e$  and optical depth  $\tau$ . For the two thermal components the  $\tau$  parameter was linked as, presumably, both undergo scattering by the same  $e^{\pm}$  population. The fit of a two-component Comptonized blackbody also exhibits significant residuals at lower energies, which can be accounted for by the addition of a cool blackbody component.

As expected,  $kT_e$  and  $\tau$  are strongly correlated, resulting in acceptable fits over a wide range of the two parameters. Given that we expect  $kT_e$  to be much larger than  $kT$ , the particular choice of  $kT_e$  and the details of the energy distribution of the scattering  $e^{\pm}$  have little impact on the outcome of the X-ray spectral fits. Note that the inferred optical depth requires a particle density in the magnetosphere (from the surface to the light cylinder 275 km above the surface) above the polar caps to be  $\sim 10^{4-6}$  times the Goldreich–Julian density. It is interesting to note that this value is comparable to that required for PSR J0737–3039A to explain the observed radio eclipses in the double pulsar system (Lyutikov 2004; Arons et al. 2005).

### 5. PHASE-RESOLVED SPECTROSCOPY

The sizable collection of source photons in the pn dataset permits an analysis of the pulsar spectrum as a function of pulse phase. To this end, I have divided the pn photons in the 0.5–3 keV range into four phase intervals, with the first interval centered on the pulse peak (see Figure 2). Due to the overwhelming background, the pn data above  $\sim 3$  keV was excluded from the analysis. Moreover, as recommended by the XMM-Newton Science Support Center, photons below 0.5 keV were ignored in order to remove electronic noise artifacts seen

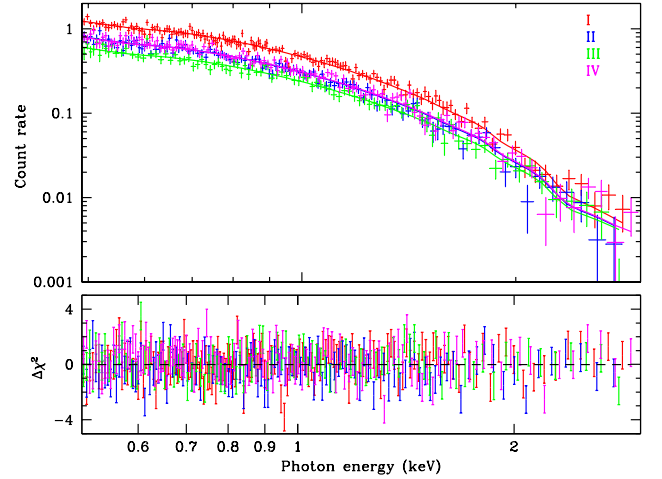


FIG. 4.— The *XMM-Newton* X-ray EPIC pn phase-resolved spectra of PSR J0437–4715 fitted with a H atmosphere model (solid lines). The phase intervals used are shown in Figure 3. The bottom panel shows the fit residuals. The Roman numerals correspond to the phase intervals shown in Figure 2.

in fast timing mode. Above this energy, the importance of the cool thermal component seen in the MOS spectra is negligible (as evident from the bottom panel of Figure 3). Therefore, only two thermal components plus the non-thermal component are used. This choice of energy cut also has the consequence of making the fits nearly insensitive to  $N_{\text{H}}$ . As evident from Table 2, the power-law component is also poorly constrained since the 0.5–3 keV band is strongly dominated by thermal emission.

The spectral fits were performed on all four spectra simultaneously. For the blackbody fits, the spectra were fit with the same temperature, while allowing for the flux normalization to vary independently for each spectrum. In the case of the H atmosphere, all parameters, including the flux normalization, were fitted jointly among the four spectra since the pulse phase dependence of the geometric projection of the emission area is taken into account internally by the model for a given set of  $M/R$ ,  $\alpha$ , and  $\zeta$ . In other words, the flux normalization in this case represents the true, deprojected area (as measured at the stellar surface), which is the same at all phases. This was accomplished by taking advantage of a functionality in `XSPEC` that permits simultaneous fitting of

phase-resolved spectra<sup>6</sup>. In addition to the anisotropic emission pattern, an important distinction of the H atmosphere model from a blackbody is the angular dependence of the emergent spectrum. In particular, the continuum emission becomes softer for larger angles with respect to the surface normal as a consequence of the temperature gradient within the atmosphere. Observationally, this property should appear as a shift in the peak of the spectrum to lower energies (see, e.g., Figure 2 in Bogdanov et al. 2007). Therefore, it is essential to properly account for the geometry to ensure an accurate measurement of the effective temperature of the radiation. Furthermore, since the emission area is observed in projection it is important to correct for this effect.

The results of the phase-resolved spectroscopic analysis are summarized in Table 2. It is important to note that (as shown in previous studies Zavlin & Pavlov 1998; Bogdanov et al. 2007), although the blackbody model can reproduce the spectral shapes of this pulsar’s phase-resolved spectra for the same temperature, the implied variations in the effective area cannot be explained by a rotating hot spot model. This lends further support for anisotropic thermal emission, which, in turn, implies the presence of an atmosphere on the surface of PSR J0437–4715.

## 6. CONSTRAINTS ON THE NEUTRON STAR COMPACTNESS

The observed pulsations of the surface thermal emission from PSR J0437–4715 contain valuable information regarding the NS compactness, which can be extracted via a constraint on the stellar mass-radius relation. To this end, I consider the model from Bogdanov et al. (2007), which assumes a rotating compact NS with two identical hot spots, each corresponding to one of the magnetic polar caps. As in the spectroscopic analysis, each polar cap is assumed to consist of a small high-temperature hot spot surrounded by a cooler annular region. The model considers a non-rotating Schwarzschild metric and incorporates the relativistic Doppler effect and propagation time delays using the prescription described in Beloborodov (2002), Poutanen & Gierliński (2003), Viironen & Poutanen (2004), and Poutanen & Beloborodov (2006). This approach is remarkably accurate as long as  $P \gtrsim 3$  ms (Cadeau et al. 2007; Morsink et al. 2007), making it applicable to PSR J0437–4715. The NS surface is assumed to be covered by a non-magnetic, optically-thick H atmosphere (Romani 1987; Zavlin et al. 1996; McClintock et al. 2004). To allow direct comparison with the data, the model was convolved with the EPIC pn plus thin filter effective area and corrected for the encircled energy fraction and the background level.

The X-ray pulse profile was fitted by considering ten parameters: the two temperatures and effective radii of each hot spot ( $T_1$ ,  $T_2$ ,  $R_1$ , and  $R_2$ ), the angles  $\alpha$  and  $\zeta$ , the NS radius  $R$ , the displacement (in degrees) of the secondary hot spot from the expected antipodal position ( $\Delta\alpha$  and  $\Delta\phi$ ), and the phase  $\phi$  of the main pulse. High-precision radio timing observations have measured the orbital inclination of the J0437–4715 binary system to

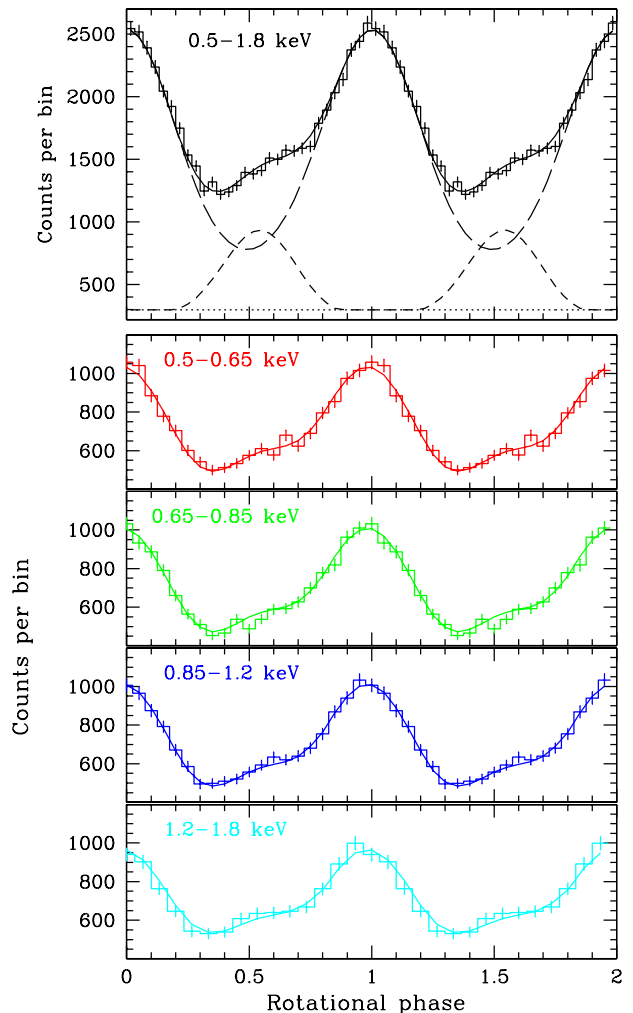


FIG. 5.— (Top panel) The XMM-Newton EPIC pn pulse profile in the 0.5–1.8 keV range with the best fit model (solid line). The individual contributions from each polar cap are shown with the dashed lines. The dotted line shows the background level. (Bottom four panels) XMM-Newton EPIC pn pulse profiles of PSR J0437–4715 in the 0.5–0.65, 0.65–0.85, 0.85–1.2, and 1.2–1.8 keV bands (from top to bottom, respectively) fitted with a model of a rotating neutron star with two-temperature H atmosphere polar caps. See text for best fit parameters.

be  $i = 137.6^\circ$  (Verbiest et al. 2008). It is very likely that the rotation axis of the MSP has aligned with the orbital angular momentum vector as the NS was spun-up during the low-mass X-ray binary stage of its evolution. This scenario implies  $\zeta \approx 137.6^\circ$  or, equivalently,  $\zeta \approx 42.4^\circ$ . Therefore, I fix the value of  $\zeta$  to the latter value. The H absorption column along the line of sight was set to  $N_H = 7 \times 10^{19} \text{ cm}^{-2}$ , while the distance was fixed at 156.3 pc (Deller et al. 2008). For all intents and purposes the 0.8% uncertainty in the parallax distance is completely negligible. Varying  $N_H$  over the range  $(1 - 10) \times 10^{19} \text{ cm}^{-2}$  results in virtually no change in the fit since its effect is unimportant above 0.5 keV. In the analysis, I assumed a fixed mass and allowed  $R$  to vary. The procedure was repeated for  $M = 0.7, 1.0, 1.3, 1.76$  and  $2.2 M_\odot$ . The fit was conducted simultaneously for four photon energy ranges (0.5 – 0.65 keV, 0.65 – 0.85 keV, 0.85 – 1.2 keV, and 1.2 – 1.8 keV) in order to weaken any covari-

<sup>6</sup> See <http://heasarc.nasa.gov/xanadu/xspec/manual1/> for further details.

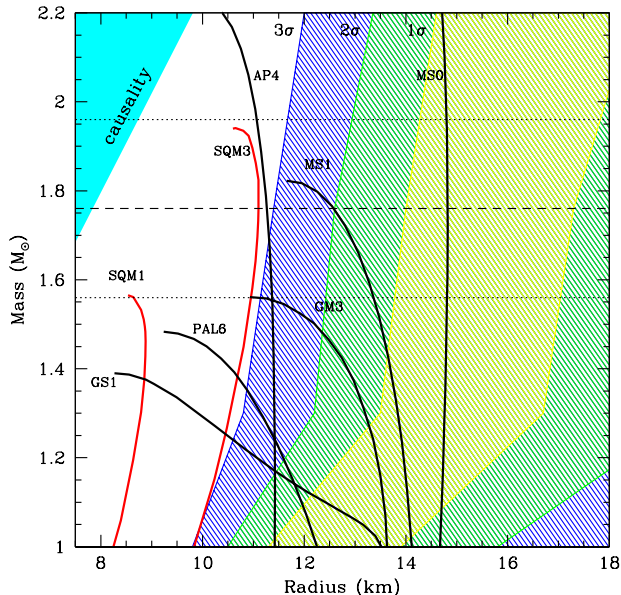


FIG. 6.— The mass-radius plane for neutron stars showing the 1, 2, and  $3\sigma$  confidence contours (yellow, green, and blue hatched regions, respectively) for PSR J0437–4715. The solid lines are representative theoretical model tracks (from Lattimer & Prakash 2004). The horizontal lines show the pulsar mass measurement from radio timing (dashed line) and the associated  $1\sigma$  uncertainties (dotted lines) from Verbiest et al. (2008).

ance between the parameters that define the emission spectrum (temperatures and effective radii) from the geometric and relativistic parameters, which do not depend on energy. The energy ranges were chosen in such a way as to yield comparable numbers of photons for all bands and to reduce the contribution of background photons. To include the non-thermal component seen in the total spectrum, I absorbed the expected number of photons per bin into the uncertainties, assuming an unpulsed contribution and a  $\Gamma = 1.56$  powerlaw spectrum. The best fit values for each parameter were determined by searching the  $\chi^2$  space. To ensure that these values are the true absolute minima of the parameter space, the procedure was repeated for a wide range of initial values for each parameter. Due to the complicated topology of the parameter space, the confidence intervals of the best fit parameters were determined by way of Monte Carlo simulations, using  $5 \times 10^3$  realizations for each of the four assumed NS masses.

The best fits to the X-ray pulsations for the H atmosphere hot spot model are shown in Figure 5. The plotted best fit yields  $\chi^2_\nu = 0.9$  for 65 degrees of freedom. As seen previously, unlike a blackbody model, H atmosphere emission can account for the morphology of the X-ray pulsations and large amplitude remarkably well. In comparison with the modeling in Bogdanov et al. (2007), the best fit shown in Figure 5 confirms the upward inflection in the lightcurve around phases 0.5–0.75, which appears to arise due to the secondary hot spot. Figure 6 shows the  $M - R$  plane with representative models for different varieties of NS EOS (see Lattimer & Prakash 2001) and the limits derived for PSR J0437–4715, with the hatched areas representing the 1, 2, and  $3\sigma$  confidence regions. The NS radius is constrained to be  $> 11.1$  km at  $3\sigma$

confidence, assuming  $M = 1.76 M_\odot$  for all combinations of the other parameters. If taken in combination with the best available mass measurement from radio timing (Verbiest et al. 2008), the limits are inconsistent with all but the stiffest equations of state. It is interesting to note that the lower bounds on the confidence intervals are much tighter. This occurs because for more compact stars it is not possible to produce the large observed pulse amplitude, owing to the stronger gravitational bending of light effect, which acts to suppress rotation-induced modulations. In contrast, the upper bounds allow for very large stars since large-amplitude pulsations can be produced more easily for a wide range of viewing geometries.

The fits to the X-ray pulsations also yield constraints on the magnetic field configuration of PSR J0437–4715. In particular, assuming  $M = 1.76 M_\odot$ , the magnetic inclination is constrained to be  $\alpha = 36^{+4}_{-3}$  degrees (at  $1\sigma$  confidence), suggesting a significant misalignment between the magnetic and rotation axes<sup>7</sup>. The latitudinal offset of the secondary polar cap is constrained to be  $\Delta\alpha = -25^{+6}_{-4}$  degrees. As defined, a negative  $\Delta\alpha$  corresponds to a northward shift from the antipodal position. The displacement in the longitudinal direction is found to be  $\Delta\phi = -20^{+2}_{-1}$  degrees, indicating that the secondary spot trails the antipodal position with respect to the sense of rotation, as evident from the phase lag of the secondary pulse in Figure 5. Based on Equations 2 and 3 in Bogdanov et al. (2008) and assuming the nominal best fit NS radius of 13.5 km, the corresponding net offset of the secondary hot spot from the antipodal position across the NS surface is  $\sim 6$  km, while the implied displacement of the magnetic dipole axis from the stellar center is  $\Delta x \approx 3$  km.

## 7. CONCLUSION

In this paper, I have presented an analysis of the deepest X-ray observation of a radio MSP to date, namely, an *XMM-Newton* exposure of PSR J0437–4715. The data permit a significantly better characterization of the spectral continuum of this pulsar in the 0.1–10 keV band compared to previous studies. Although the observed radiation from J0437–4715 can be described well by multiple models, in all cases the vast majority of soft photons ( $\gtrsim 90\%$ ) appear to be thermal in nature. This thermal radiation exhibits at least three components, with the hottest two having total effective areas consistent with the expected polar cap size. The coolest component, on the other hand, appears to cover a significant portion of the stellar surface, consistent with findings based on UV observations (Kargaltsev et al. 2004; Durant et al. 2012). Since passive cooling of any primordial heat stored in the NS cannot account for the high global NS temperature ( $\gtrsim 10^5$  K), various heating mechanisms have been invoked to explain the excess, including: re-radiation of the energy deposited in the inner crust by polar cap heating, rotochemical heating (Fernández & Reisenegger 2005), “gravitochemical” heating caused by a time-varying gravitational constant (Jofré et al. 2006), or capture of exotic par-

<sup>7</sup> By convention,  $\alpha$  is reckoned from the spin pole towards the equator.



ticles in the NS interior (Hannestad et al. 2002). See Kargaltsev et al. (2004) and Durant et al. (2012) for further discussions of the various possible heating mechanisms that may operate in PSR J0437–4715.

An important goal of future observations will be to establish the true nature of the hard photons ( $\gtrsim 3$  keV) from PSR J0437–4715. This can be best accomplished through detailed phase-resolved spectroscopy. Better characterization of the optical and  $\gamma$ -ray emission from this pulsar may offer additional clues into the nature of this radiation. In addition, with the recent launch of NuSTAR<sup>8</sup>, a hard X-ray focusing telescope covering the 6–79 keV range, further insight could be gained into the connection between the harder X-ray and  $\gamma$ -ray emission from this pulsar.

For the first time, I conduct phase-resolved X-ray spectroscopy of a radio pulsar that correctly accounts for the system geometry and the radiation pattern of the atmosphere by jointly fitting the spectra from all phase intervals. With greatly increased photon statistics, this potentially powerful approach can yield stringent constraints on the NS parameters by utilizing a two-dimensional approach to spectroscopy in the photon energy–pulse phase plane.

The model pulse profiles in Figure 5 imply a significant offset of the secondary hot spot from the antipodal position, which in turn, suggest deviation from the standard centered magnetic dipole configuration. As demonstrated by Harding & Muslimov (2011), even a slight azimuthally asymmetric displacement of the pulsar magnetic field can substantially amplify the accelerating electric field on one side of the polar cap, which when combined with a smaller field line radius of curvature, leads to larger pair multiplicity. As a consequence, the death line for producing  $e^\pm$  by curvature radiation shifts downward in the period-period derivative diagram, resulting in a larger number of pulsars having high pair multiplicities. If common among MSPs, and pulsars in general, these magnetic field distortions could have profound implications for studies of the pulsar population, modelling high energy pulsed radiation, and constraining the pulsar contribution to cosmic ray positrons.

The analysis presented herein confirms that the X-ray pulsed fraction of PSR J0437–4715 is consistent with

the existence of an atmospheric layer on the NS surface and cannot be reproduced by a blackbody. Modelling of the thermal pulsations gives a limit on the NS radius of  $> 11.1$  km ( $3\sigma$  conf.) assuming a mass of  $1.76 M_\odot$ . This lower bound is much stricter compared to the limit obtained from the shallower archival observations. This value is in agreement with several NS radius measurements using quiescent low-mass X-ray binaries (e.g., Rutledge et al. 2001; Heinke et al. 2006; Webb & Barret 2007) and X-ray bursts (see, e.g., Özel 2006; Özel et al. 2010). However, it is important to emphasize that these methods have resulted in a wide range of often contradictory constraints on the NS radius (see, e.g., Suleimanov et al. 2011; Özel et al. 2012, for the case of X-ray bursts). This highlights the clear need to investigate the systematic uncertainties and reliability of these model-dependent approaches to constraining NS structure, including the method employed in this present paper.

This issue notwithstanding, as demonstrated in Bogdanov et al. (2008), deeper X-ray observations of PSR J0437–4715 should result in even stricter constraints on  $M/R$ , especially when combined with further refinement in the NS mass measurement from radio timing and joint modelling of the pulsed X-ray and  $\gamma$ -ray emission (see, e.g., Venter et al. 2009) to better constrain the system geometry. Such efforts may produce definitive measurements of the  $M - R$  relation, and by extension, the state of cold, dense matter.

I thank Z. Arzoumanian and V. Kaspi for numerous insightful discussions. This research was supported in part by a Canadian Institute for Advanced Research Junior Fellowship. The work presented was based on observations obtained with *XMM-Newton*, an ESA science mission with instruments and contributions directly funded by ESA Member States and NASA. The research in this paper has made use of the NASA Astrophysics Data System (ADS).

Facilities: *XMM-Newton* (EPIC)

## REFERENCES

- Abdo, A. A., et al. 2009, *Science*, 325, 848  
 Alpar, M. A., Cheng, A. F., M. A. Ruderman, M. A., & Shaham, J. 1982, *Nature*, 300, 728  
 Archibald, A. M., Kaspi, V. M., Bogdanov, S., Hessels, J. W. T., Stairs, I. H., Ransom, S. M., McLaughlin, M. A., & Lorimer, D. 2010, *ApJ*, 722, 88  
 Arons, J., Backer, D. C., Spitkovsky, A., Kaspi, V. M. 2005, *ASPC*, 328, 95  
 Bailyn, C. D. 1993, *ApJ*, 411, L83  
 Becker, W. & Trümper, J. 1993, *Nature*, 365, 528  
 Becker, W. & Trümper, J. 1999, *ApJ*, 341, 803  
 Becker, W. & Aschenbach, B. 2002, *Proceedings of the 270. WE-Heraeus Seminar on Neutron Stars, Pulsars, and Supernova Remnants*, Eds. W. Becker, H. Lech, J. Trümper, p. 64  
 Beloborodov, A. M. 2002, *ApJ*, 566, 85  
 Bogdanov, S., Grindlay, J. E., & Rybicki, G. B. 2006, *ApJ*, 648, L55  
 Bogdanov, S., Rybicki, G. B., & Grindlay, J. E. 2007, *ApJ*, 670, 668  
 Bogdanov, S., Grindlay, J. E., & Rybicki, G. B. 2008, *ApJ*, 689, 407  
 Bogdanov, S., & Grindlay, J. E. 2009, *ApJ*, 703, 1557  
 Braje, T. M., Romani, R. W., & Rauch, K. P. 2000, *ApJ*, 531, 447  
 Cadeau, C., Morsink, S. M., Leahy, D., & Campbell, S. S. 2007, *ApJ*, 654, 458  
 Deller, A. T., Verbiest, J. P. W., Tingay, S. J., Bailes, M. 2008, *ApJ*, 685, L67  
 Durant, M., Kargaltsev, O., Pavlov, G. G., Kowalski, P. M., Posselt, B., van Kerkwijk, M. H., Kaplan, D. L. 2012, *ApJ*, 746, 6  
 Fernández, R., & Reisenegger, A. 2005, *ApJ*, 625, 291  
 Halpern, J. P., Martin, C., Marshall, H. L. 1996, *ApJ*, 462, 908  
 Halpern, J. P. & Marshall, H. L. 1996, *ApJ*, 464, 760  
 Hannestad, S., Keränen, P., & Sannino, F. 2002, *PhRvD*, 66, 045002  
 Harding, A. K. & Muslimov, A. G. 2002, *ApJ*, 568, 862  
 Harding, A. K. & Muslimov, A. G. 2011, *ApJ*, 726, 10  
 Heinke, C. O., Rybicki, G. B., Narayan, R., & Grindlay, J. E. 2006, *ApJ*, 644, 1090  
 Jofré, P., Reisenegger, A., & Fernández, R. 2006, *PhRvL*, 97, 1102  
 Johnston, S., Lorimer, D. R., Harrison, P. A., Bailes, M., Lyne, A. G., Bell, J. F., Kaspi, V. M., Manchester, R. N., D’Amico, N., & Nicastro, L. 1993, *Nature*, 361, 613

<sup>8</sup> <http://www.nustar.caltech.edu/home>

- Kargaltsev, O., Pavlov, G. G., & Romani, R. W. 2004, *ApJ*, 602, 327
- Lattimer, J. M. & Prakash, M. 2001, *ApJ*, 550, 426
- Lyutikov, M. 2004, *MNRAS*, 353, 1095
- McClintock, J. E., Narayan, R., & Rybicki, G. B. 2004, *ApJ*, 615, 402
- Morsink, S. M., Leahy, D. A., Cadeau, C., Braga, J. 2007, *ApJ*, 663, 1244
- Nishimura, J., Mitsuda, K., & Itoh, M. 1986, *PASJ*, 38, 819
- Özel, F. 2006, *Nature*, 441, 1115
- Özel, F., Baym, G., & Güver, T. 2010, *PhRvD*, 82, 101301
- Özel, F., Gould, A., & Güver, T. 2012, *ApJ*, 748, 5
- Pavlov, G. G. & Zavlin, V. E. 1997, *ApJ*, 490, L91
- Poutanen, J., Beloborodov, A. M. 2006, *MNRAS*, 373, 836
- Poutanen, J., & Gierliński, M. 2003, *MNRAS*, 343, 1301
- Psaltis, D., Özel, F., & DeDeo, S. 2000, *ApJ*, 544, 390
- Romani, R. W. 1987, *ApJ*, 313, 718
- Rutledge, R. E., Bildsten, L., Brown, E. F., Pavlov, G. G., & Zavlin, V. E. 2001, *ApJ*, 551, 921
- Schaab, Ch., Sedrakian, A., Weber, F., & Weigel, M. K. 1999, *A&A*, 346, 465
- Suleimanov, V., Poutanen, J., Revnivtsev, M., & Werner, K. 2011, *ApJ*, 742, 122
- Venter, C., Harding, A. K., & Guillemot, L. 2009, *ApJ*, 707, 800
- Verbiest, J. P. W., Bailes, M., van Straten, W., Hobbs, G. B., Edwards, R. T., Manchester, R. N., Bhat, N. D. R., Sarkissian, J. M., Jacoby, B. A., Kulkarni, S. R. 2008, *ApJ*, 679, 675
- Viironen, K., & Poutanen, J. 2004, *A&A*, 426, 985
- Webb, N. A., & Barret, D. 2007, *ApJ*, 671, 727
- Zavlin, V. E., Pavlov, G. G., & Shibanov, Yu. A. 1996, *A&A*, 315, 141
- Zavlin, V. E. & Pavlov, G. G. 1998, *A&A*, 329, 583
- Zavlin, V. E., Pavlov, G. G., Sanwal, D., Manchester, R. N., Trümper, J., Halpern, J. P., & Becker, W. 2002, *ApJ*, 569, 894
- Zavlin, V. E. 2006, *ApJ*, 638, 951
- Zhang, L., & Cheng, K. S. 2003, *A&A*, 398, 639